

This is an Open Access document downloaded from ORCA, Cardiff University's institutional repository: <https://orca.cardiff.ac.uk/id/eprint/137085/>

This is the author's version of a work that was submitted to / accepted for publication.

Citation for final published version:

Dong, Boliang, Xia, Junqiang, Zhou, Meirong, Deng, Shanshan, Ahmadian, Reza and Falconer, Roger A. 2021. Experimental and numerical model studies on flash flood inundation processes over a typical urban street. *Advances in Water Resources* 147 , 103824. 10.1016/j.advwatres.2020.103824

Publishers page: <http://dx.doi.org/10.1016/j.advwatres.2020.103824>

Please note:

Changes made as a result of publishing processes such as copy-editing, formatting and page numbers may not be reflected in this version. For the definitive version of this publication, please refer to the published source. You are advised to consult the publisher's version if you wish to cite this paper.

This version is being made available in accordance with publisher policies. See <http://orca.cf.ac.uk/policies.html> for usage policies. Copyright and moral rights for publications made available in ORCA are retained by the copyright holders.



Experimental and numerical studies on flood inundation processes over a typical urban street

Boliang Dong¹, Junqiang Xia*¹, Meirong Zhou¹, Shanshan Deng¹,
Reza Ahmadian², Roger A. Falconer²

1 State Key Laboratory of Water Resources and Hydropower Engineering Science, Wuhan University, Wuhan
430072, China; Email: xiajq@whu.edu.cn

2 School of Engineering, Cardiff University, Cardiff, CF24 3AA, UK

Abstract:

Accurate prediction of flood inundation processes in urban areas is challenging due to the complexity of street layouts and the variety of infrastructures. In this study, based on a laboratory model of urban flooding with a sewer system underneath, a series of laboratory experiments were conducted to investigate the influences of different street layouts and infrastructures on flood inundation processes. Key hydrographs of water depth and flow velocity were recorded at several measurement points to provide comprehensive information about the hydrodynamic characteristics of urban flooding. Furthermore, a 2D shallow water equations model based on the finite volume method was also utilized to replicate the experimental scenarios considered. An analysis of the mesh resolution and discharge capacity formulae for street inlets were also performed through a series of numerical tests. The following conclusions are drawn from this study: (i) the sewer system has a strong influence on the flood inundation processes in terms of reducing both the surface water depth and flood wave velocity, as compared with street layouts and other infrastructures; (ii) the results from the numerical simulations agree well with the experimental findings, with the NSE values being greater than 0.9 and the RMSE values less than 1.5×10^{-3} ; (iii) the marginal effect of increasing the mesh resolution is significant, which means a further increment in the mesh resolution may benefit slightly the numerical model predictions, but at the expense of an increasing computational cost; and

29 (iv) of all the inlet discharge capacity formulae used in this study, the weir and orifice formulae
30 considering the influence of rain boxes were the most appropriate for representing the geometric
31 features of street inlets and showed the best performance in calculating the flow exchange between
32 surface runoff and underground sewer system.

33 **Keywords:** Urban flood, flood inundation, laboratory experiments, numerical modelling, street inlets,
34 inlet discharge capacity formulae

35

36 **1 Introduction**

37 Flooding is the most common natural disaster world-wide and has become a major threat to
38 people and property in urban areas. The frequency of occurrence and intensity of urban flood events
39 are rising gradually, due to global climate change, increasing population and rapid urbanization. From
40 1995 to 2015, nearly half of the natural disasters globally were associated with floods, leading to 56%
41 of the total number of victims suffering from any type of natural disaster (UNDRR, 2019). For
42 example, 14 people died and 2,3600 buildings were destroyed in a recent extreme flood event in
43 Wuhan City, China, with 757,000 people being affected as a result of the 2016 flood event (Cheng et
44 al., 2019). Therefore, it is important to understand the causes and consequences of urban flooding and
45 to develop accurate modelling methods for predicting the flood inundation processes in urban regions.

46 Field data for urban floods, such as aerial photography and watermarks, are generally insufficient
47 for accurate model validation and such data are limited in representing the complexity of flood
48 inundation extent, particularly for extreme flood events (Puech and Raclot, 2002; Chen et al., 2017).
49 In recent years, a series of experimental studies have been undertaken to better understand flood
50 inundation processes, as well as the interaction between floodwaters and infrastructures in urban areas
51 (Mignot et al., 2019). In addition, these experimental studies have provided a reliable dataset for the

52 validation of numerical models. Water depth and flow velocity are the key parameters to describe the
53 characteristics and disaster-causing mechanisms of urban flooding. In most laboratory experimental
54 studies, the results are acquired by using several water gauges and/or well-established sensing
55 techniques, such as PIV (Particle Image Velocimetry) and RGB-D (red-green-blue-depth) (Soares-
56 Frazão and Zech, 2007; Aureli et al., 2015; Martínez-Aranda et al., 2018). In comparison to using a
57 limited number of gauges, sensing techniques are more capable of reconstructing the overall features
58 of the velocity field and the water level distribution. However, for large-scale and complex laboratory
59 experiments, sensing techniques have a number of shortcomings, such as the limited visual angle and
60 object occlusion.

61 In laboratory experiments of urban flooding, the most common and accessible method to produce
62 an urban flooding process is to provide an upstream runoff, including the discharge hydrograph
63 resulting from a dam-breach event. Soares-Frazão and Zech (2007) and Aureli et al. (2015)
64 investigated the performance of an isolated building subject to a dam-break flood event, and they
65 conducted detailed measurements on the variation in flow pattern around the building. Further
66 experimental studies on the flood inundation processes in idealized urban areas were conducted by
67 Testa et al. (2007), Soares-Frazão and Zech (2008), and LaRocque et al. (2013). In these studies, it
68 was found that the key flood characteristics, such as flow path, velocity field and water depth
69 distribution, can be strongly influenced by the complex street layout of an urban area. The layout of
70 a city is organized based on streets, and the natural topography is usually blocked by buildings and
71 greenbelts. Therefore, urban streets become the main flow paths during flooding events (Mignot et
72 al., 2006, 2013; Lee et al., 2016; Chen et al., 2018). Instead of focusing only on the pattern of surface
73 flow, some researchers have investigated the flow exchange between surface runoff and underground
74 pipe flow, via street inlets and manholes etc. (Noh et al., 2016; Rubinato et al., 2017; Martins et al.,

75 2018). Previous laboratory experiments of urban flooding with sewer systems have focused on the
76 hydraulic efficiency of street inlets (Gómez et al., 2011, 2013; Rubinato et al., 2017) and the
77 interaction between surface runoff and sewer pipe flow (Bazin et al., 2014; Fraga et al., 2017), as well
78 as sediment and pollutant transport during rainfall events (Naves et al., 2020). Most of the existing
79 urban flood experiments reported in the literature for real street layouts and underground sewer
80 systems have mainly concentrated on studying steady-state and gradually varying flow patterns, with
81 few studies investigating unsteady flood inundation processes.

82 In addition to laboratory studies, numerical modelling nowadays provides the main tool used to
83 predict the inundation extent of urban floods and has become the key tool to plan for disaster
84 prevention and to undertake scientific investigations. Accurate modelling of real urban flood events
85 needs to deal with irregular topographies, capture wet and dry fronts, and provide accurate predictions
86 of transcritical flood events. Among the existing numerical models of urban flooding, the shallow
87 water equations (SWEs) are solved within these models, achieving a balance between model accuracy
88 and computational efficiency. A solution of the SWEs, based on the Godunov-type finite volume
89 method, can satisfy the hyperbolic nature of the SWEs and capture discontinuities in the flow field,
90 such as those characteristic hydraulic jumps. Therefore, this method is now one of the most popular
91 numerical schemes used for modelling extreme flood events. Ghostine et al. (2009) adopted two
92 different SWEs models and the more sophisticated model of FLUENT to simulate supercritical flows
93 at street junctions, with the results indicating that the second-order SWEs model is capable of
94 predicting the complex flow patterns occurring during urban flood events.

95 The increase of impervious surfaces in urban regions generally reduces the infiltration rate and
96 causes higher surface runoff, which then leads to higher flood risks in these areas (Shao et al., 2019;
97 Ferreira et al., 2019). In this situation, sewer systems act as the main infrastructure to drain away the

98 surface runoff during extreme rainfall events. Many dual-drainage models have been developed to
99 achieve simultaneous simulation of the complex processes, involving both ground surface flow and
100 underground pipe flow (Leandro et al., 2009; Seyoum et al., 2012; Jang et al., 2018). In most of the
101 dual-drainage models, the surface flow is calculated by solving the 2D SWEs, while the sewer flow
102 is simulated by solving the 1D pipe flow equations. The transition of flow regime in sewer pipes is
103 captured by adopting additional techniques, such as the Preissmann slot approach (PSA) and the two-
104 component pressure approach (TPA) (Vasconcelos et al., 2006; Sanders and Bradford, 2011; Li et al.,
105 2020). The drainage discharge between the ground surface and drainage pipes can be calculated using
106 weir and/or orifice formulae (Rubinato et al., 2018). However, most of the inlet capacity formulae are
107 derived from steady-state experiments (Gómez et al., 2011, 2013; Lee et al., 2012), and the application
108 of these formulae in simulating highly unsteady urban flood events is a potential source of key
109 uncertainties.

110 The current study is organized into five parts. Section 2 describes the experimental facility and
111 the corresponding measurement procedure, together with the numerical modeling framework. Section
112 3 reports the results obtained from laboratory experiments and numerical modelling simulations, with
113 the main impacts on the flood inundation processes being the initial water depth, different street
114 layouts, and the urban sewer system. Section 4 presents the discussion about the importance of mesh
115 resolution on the numerical simulations and the performance of the existing discharge capacity
116 formulae in the dual drainage modeling. The conclusions are then given in Section 5.

117 **2 Methods**

118 Investigations into flood inundation processes over an idealized urban street were performed in
119 the current study, using both generalised laboratory experiments and numerical modelling. The
120 inundation characteristics of urban flooding over a typical urban street were measured in detail,

121 covering the variations in water depth and flow velocity at different locations. Numerical modelling
122 was carried out using a 2D SWEs numerical model including appropriate inlet discharge capacity
123 formulae.

124 **2.1 Set-up of laboratory experiments**

125 2.1.1 Layout of the laboratory model

126 The experiments were conducted in a large-scale laboratory flume. The flume is 20 m long, 3 m
127 wide, 0.6 m deep, with a horizontal bed. Both the sidewalls and the flume bed are made from
128 transparent tempering glass, to facilitate observations. As illustrated in Fig. 1a, a dam composed of
129 two thin walls and a 1 m wide lift-gate separates the upstream part of the laboratory flume,
130 representing a reservoir zone. Downstream of the gate, the physical model has the layout of a real
131 urban street. Various infrastructures are included in the model, including a road, buildings, greenbelt
132 sections, sidewalks and an underground sewer system. The physical model was designed according
133 to the law of Froude similarity, with a scale of one tenth to the modelled real-world scenario.

134 **Insert Fig. 1**

135 Each building in this study is 0.8 m long, 0.4 m wide, and 0.5 m high, designed according to the
136 size of a widely used house in China. The model main road and sidewalk have a width of 1.2 m and
137 0.3 m, respectively. In addition, the model sidewalk level is 1 cm higher than the level of the model
138 road. Ten street inlets are distributed along the left and right sides of the road (viewing downstream),
139 with a spacing of 2 m between two consecutive street inlets. In order to describe the location of
140 measurement points and buildings, a plane cartesian coordinate system is set up in this physical model.
141 The origin of the axis is located at the lower-left corner of Fig. 1a (viewing downstream), with the
142 positive x -axis direction facing downstream and along the left side of the flume. The exact coordinates
143 of water level gauges and the centroid of two upstream buildings are given in Table 1. The model has

144 a free overflow at the end and the downstream boundary can therefore be treated as an open boundary
145 in the numerical model.

146 **Insert Table 1**

147 As shown in Fig. 1b, the model has a two-layer structure, and the underground sewer system is
148 linked to the road surface via street inlets. The street inlets used in this study have a rectangular plan
149 view, with a size of 10 cm × 20 cm, and the void ratio of the inlet grate is 28% (Fig. 1c). Both the
150 side tubes and main pipes are made from acrylic pipes, with the corresponding inner diameters being
151 2.2 and 20.0 cm. A side tube is connected to a rain box with the size of 200×100×150 mm. The main
152 sewer pipe has a longitudinal slope of 2/1000, and the upstream and downstream ends of the pipe are
153 linked with a laboratory pump and a water tower respectively, to control the corresponding boundary
154 conditions. Due to the water head difference along the sewer system, the overland flow drains from
155 the ground surface to the main pipe through the street inlets. As the dam-break flow is very intense
156 and highly unsteady, the exchange discharge through the street inlets into the sewer network also
157 varies significantly, which makes the downstream water depth in the main pipe hard to control. In
158 order to eliminate the uncertainties caused by the downstream boundary, the gate of the water tower
159 remained open during the experiments. Accordingly, the downstream end of the main pipe would be
160 treated as an open boundary. Besides, the upstream discharge of the main pipe was zero in all the
161 cases reported herein, and the upstream boundary of the main pipe would be treated as a solid wall
162 boundary condition.

163 2.1.2 Experimental procedure

164 At the start of each experiment, a pump was first used to fill the upstream reservoir from the
165 laboratory water tank. After the water level in the reservoir was still, the experiment was commenced
166 by lifting the gate quickly. It is known that dam failure is a very rapid process, and the time taken in

167 lifting the gate has a strong influence on the corresponding experimental results. Lauber and Hager
168 (1998) proposed a gate opening criteria for the maximum gate opening time to minimize the errors
169 caused by the gate opening process. von Hafen et al. (2019) used a smoothed particle hydrodynamics
170 (SPH) model to evaluate this criterion, with the results indicating that the Lauber and Hager gate
171 opening criterion leads to an error of less than 1%, as compared with instantaneously opening the
172 gate. In this study, a high-speed camera was used to record the gate opening time, which can guarantee
173 that the Lauber and Hager criterion was fully satisfied.

174 Many unforeseen factors affect the flood inundation processes, and it is therefore impossible to
175 obtain exactly the same results between identical experimental runs. Therefore, each experimental
176 run was carried out at least twice to reduce the influence of unforeseen factors and ensure
177 experimental repeatability as closely as possible. Table 2 presents a summary of all the experimental
178 runs, and the current study covered 18 tests with different combinations of street structure and initial
179 water depth. Case 1 was performed to investigate the idealized flood inundation with only the
180 sidewalks being set up in the flume. Case 2 was intended to identify the influence of buildings on the
181 flood inundation processes. Case 3 investigated the influence of urban greenbelts. Case 4 shortened
182 the distance between buildings and increased the number of buildings to reveal the influence of
183 building density. Cases 5 and 6 were used for investigating the mitigation effect of an urban drainage
184 system. Each case was conducted using initial water depths of 10, 20, and 30 cm to reveal the
185 relationship between flood intensity and initial water depth.

186 **Insert Table 2**

187 2.1.3 Flow measurements

188 The temporal variations in water levels were recorded at seven measurement points, using
189 ultrasonic water level gauges. The water level gauges have a sampling frequency of 4 Hz, with a

190 measurement accuracy of about ± 0.2 mm. The measurement points (i.e. P1, P2, P5, P6, and P7) are
191 located along the centerline of the flume to record the flood routing characteristics. Measurement
192 points P3 and P4 are located at the upstream and downstream side of the first building, to record the
193 temporal variations in water levels around the first building. The flow velocities at points P2, P4, and
194 P7 were measured using a 2D electromagnetic velocity meter. In comparison to using the acoustic
195 doppler velocity meter (ADV), the electromagnetic velocity meter can measure the instantaneous
196 flow velocity in relatively shallow water depths. However, the water depth was too shallow to give
197 detailed measurements of the velocity profiles along the vertical axis throughout the experiments.
198 Therefore, only one point velocity was measured along the vertical direction at each measurement
199 site, with the sensor being fixed at a height of 1.5 cm above the flume bottom. The sampling frequency
200 of the velocity meter was set to 100 Hz to provide high-resolution results. Calibrated electromagnetic
201 flowmeters were installed on each side tube to record the drainage discharge from the ground surface
202 to the sewer system.

203 **2.2 Framework of the numerical model**

204 2.2.1 2D shallow water equations

205 Mathematical models are essential tools for simulating and evaluating urban flood inundation
206 processes. Apart from complicated and computationally expensive three-dimensional models, 2D
207 SWEs models achieve a good balance between model accuracy and computational efficiency.
208 Therefore, SWEs models are widely used to simulate urban floods, with complex water depth
209 distributions and velocity patterns. In this study, a 2D model is adopted, based on the finite volume
210 method used to solve the SWEs (Xia et al., 2011). The governing equations of the current model can
211 be written in the following conservative form:

$$\frac{\partial \mathbf{U}}{\partial t} + \frac{\partial \mathbf{F}(\mathbf{U})}{\partial x} + \frac{\partial \mathbf{G}(\mathbf{U})}{\partial y} = \mathbf{S} \quad (1)$$

212 where the vector of conserved variables:

$$\mathbf{U} = (h, hu, hv)^T \quad (2)$$

213 where h is the water depth; and u and v are the depth-averaged velocity components in the x - and y -
214 coordinate directions. The flux vectors of these conserved variables are:

$$\mathbf{F} = (hu, hu^2 + \frac{1}{2} gh^2, huv)^T; \quad \mathbf{G} = (hv, huv, hv^2 + \frac{1}{2} gh^2)^T \quad (3)$$

215 The source term, including the bed slope, friction stress and drainage discharge, can be expressed
216 by:

$$\mathbf{S} = (-q_L, gh(S_{0x} - S_{fx}), gh(S_{0y} - S_{fy}))^T \quad (4)$$

217 where q_L is the drainage discharge per unit area; and the bed slope terms S_{0x} and S_{0y} account for the
218 variation of the terrain elevation z_b (m) in the x and y directions, as given by:

$$S_{0x} = -\partial z_b / \partial x; \quad S_{0y} = -\partial z_b / \partial y \quad (5)$$

219 The bed friction terms S_{fx} and S_{fy} in the x and y directions can be formulated respectively as follows:

$$S_{fx} = n^2 u \sqrt{u^2 + v^2} / h^{4/3}; \quad S_{fy} = n^2 v \sqrt{u^2 + v^2} / h^{4/3} \quad (6)$$

220 where n is the Manning roughness coefficient ($\text{s.m}^{-1/3}$).

221 2.2.2 Discharge capacity formulae for street inlets

222 As the major interconnection between the ground surface and the underground sewer system,
223 street inlets play an important role in flood mitigation in urban areas. Using accurate discharge
224 capacity formulae for street inlets is crucial to the improvement of the prediction accuracy of a
225 numerical model. In this study, two kinds of inlet discharge capacity formulae were selected for
226 comparison and evaluation, including the most frequently used weir and orifice formulae and the
227 unified discharge capacity formula. Details of each approach are given below:

228 (i) Weir and orifice formulae for discharge capacity of street inlets

229 The sketch of the drainage between surface runoff and sewer pipe flow is shown in Fig. 2. In
230 general, the drainage states of a street inlet can be generally divided into non-submerged and
231 submerged conditions, which are governed respectively by the weir and orifice formulae. Weir and
232 orifice formulae are the most widely accepted formulae for calculating the exchange discharge
233 through manholes and street inlets (Noh et al., 2016; Fraga et al., 2017). According to the hydraulic
234 status of street inlets, the exchange discharge from the surface to the rain box (Q_i) can be determined
235 as follows:

$$Q_i = \begin{cases} C_{iw} \times \frac{2}{3} \times L \sqrt{2g} (h_{ti})^{3/2} & \text{Non-submerged} \\ C_{io} \times A_i \sqrt{2gh_{ti}} & \text{Submerged} \end{cases} \quad (7)$$

236 where h_{ti} is the total hydraulic head, and $h_{ti} = h_s + u_i^2 / 2g$; h_s is the surface water depth; u_i is the
237 incoming surface flow velocity; A_i is the area of the street inlet; L is the perimeter of the street inlet;
238 and C_{iw} and C_{io} are the corresponding empirical coefficients for the weir and orifice formulae.

239 Besides the flow exchange through inlet grates, the discharge capacity of side tubes is equally
240 important. The formula for calculating the discharge from the rain box to the main pipe (Q_s) is almost
241 the same as Eq. (7b), as given by:

$$Q_s = C_{so} \times A_s \sqrt{2g(h_{ts})} \quad (8)$$

242 where $h_{ts} = h_{sp} - h_{pm} - h_{sb} + h_b$ if the rain box is ventilated, and $h_{ts} = h_{ti} + h_{sp} - h_{pm} - h_{sb} + h_b$ if the rain box is
243 pressurised; h_{sp} is the height between the ground surface and the bottom of the main pipe; $h_{pm} =$
244 $\max(h_p, d_p/2)$; h_p is the water head in the main pipe; h_{sb} is the height between the ground surface and
245 the bottom of the rain box; h_b is the water depth in the rain box; A_s is the inner area of the side tube;
246 and d_p is the diameter of the main pipe.

247 Rain boxes can store the drainage flow between the surface and the underground sewer pipe,

248 which shortens the inundation time and mitigates the flood intensity. Consequently, it is necessary to
249 take the water balance of the rain box into consideration, given below:

$$\frac{\partial h_b}{\partial t} = \frac{(Q_i - Q_s)}{A_b} \quad (9)$$

250 where A_b is the inner area of the rain box. However, some studies have been carried out without
251 considering the influence of rain boxes (Chanson et al., 2002; Lee et al., 2012; Martins et al., 2018).
252 One of the most significant shortcomings of these studies is that it is difficult to quantify the transition
253 of the discharge capacity, which is closely related to the hydraulic status of the rain box. For example,
254 the discharge capacity of the inlet grate in most cases is larger than the value of the side tube. If the
255 rain box is pressurised, then the total capacity will be restricted by the side tube. Therefore, this
256 simplification has a limited scope of application and is hard to adapt to the actual situations. The
257 performance of different formulae will be discussed in the following section, in order to quantitatively
258 reveal the uncertainties caused by different discharge capacity formulae of street inlets.

259 **Insert Fig. 2**

260 (ii) Unified formula for discharge capacity of street inlet

261 Chen et al. (2020) conducted laboratory experiments on the discharge capacity of street inlets.
262 Based on their experimental results, it was found that the ratio of the composite velocity through the
263 street inlet to the incoming flow velocity can be expressed by a power function of the incoming
264 Froude number. Therefore, a unified formula for the discharge capacity of street inlets was proposed
265 using the method of dimensional analysis. Compared with other formulae, this formula was relatively
266 simple and can be applied to different conditions regardless of hydraulic status:

$$Q_i = au_i A_i Fr^b \quad (10)$$

267 where Fr is the Froude number in front of a street inlet; and a and b are empirical coefficients.

268 2.2.3 Numerical solution

269 The finite volume method has been widely used as a reliable tool for solving the time-dependent,
270 nonlinear, hyperbolic shallow water equations. In this model, the second-order cell-centered Roe's
271 scheme is used, and accordingly the average values of the conserved variables are stored at the centre
272 of each cell. The solution of the numerical flux across the cell edge is the core of the finite volume
273 method, and the numerical flux is evaluated at the edge of two adjacent cells by means of the
274 monotone upstream scheme for conservation laws (MUSCL) (van Leer, 1979). Based on the
275 rotational invariance property of the SWEs, the calculation of the numerical flux can be treated as a
276 1D Riemann problem. Accordingly, Roe's approximate Riemann solver is used to calculate the
277 numerical flux across the edge. An improper treatment of the source terms may cause problems such
278 as a reverse in the flow direction and non-physical oscillations, especially under the condition of small
279 water depths. However, these problems can be solved by reducing the numerical time step, which
280 sometimes leads to an unacceptable computational burden. In order to improve on the numerical
281 stability of the scheme, a semi-implicit method is adopted in this model to discretize the bed friction
282 term:

$$(S_{fx}, S_{fy}) = \left[\left(n^2 \sqrt{u^2 + v^2} / h^{4/3} \right)^k (hu)^{k+1}, \left(n^2 \sqrt{u^2 + v^2} / h^{4/3} \right)^k (hv)^{k+1} \right] \quad (11)$$

283 where the superscript k denotes the time level.

284 2.2.4 Mesh generation

285 Spatial discretization of the computational domain is a precondition in any numerical model. In
286 this study, simulations were performed on unstructured triangular meshes, and fine meshes with a 5
287 cm resolution were used in order to eliminate the influence of the mesh scale. As shown in Fig. 3,
288 unstructured meshes were implemented to replicate the geometry of the model street, and the
289 building-hole method was adopted to represent buildings by setting up holes with solid wall

290 boundaries (Li et al., 2019). The Manning roughness coefficients for the model road and other parts
291 of the flume were estimated to be 0.007 and 0.012 s.m^{-1/3}, respectively. The downstream end of the
292 laboratory flume was specified as a free boundary, while the other boundaries were specified as solid
293 wall boundaries.

294 **Insert Fig. 3**

295 **3 Experimental observations and numerical simulations**

296 **3.1 General description of the experimental flood inundation processes**

297 Visual observations indicate that the flow patterns in different cases showed several common
298 characteristics. After the rapid removal of the reservoir gate, the water body in the reservoir collapsed,
299 and the extreme flood event inundated through the model street, forming a mass of shock waves. Fig.
300 4 presents the simulated profiles of the dam-break flow for Case 2. At the initial time, the water depth
301 in the upstream reservoir was 30 cm, and the threshold water depth for capturing the wet and dry front
302 was set to 1 mm. After the gate was opened, the flood wave rapidly spread over the initially dry street.
303 The numerical model predicted a surge front propagating along the downstream road, and a
304 rarefaction wave travelled toward the upstream reservoir. When the rarefaction wave reached the
305 reservoir boundary, it reflected back and led to an oscillation of the free surface. Due to the interaction
306 between the buildings and the dam-break flow, the water levels around the buildings were much
307 higher than the levels on the model road. In addition to the water depth distribution, the presence of
308 the buildings also altered the flow path and led to changes in the flow regime, which caused the
309 occurrence of hydraulic jumps in the flume.

310 **Insert Fig. 4**

311 **3.2 Effect of initial water depth on the flood inundation processes**

312 Fig. 5 indicates the temporal variations in the water level for different initial water depths for

313 Case 2. A progressive reduction in the water depth was recorded at the measurement point P1, located
314 in the upstream reservoir, and a larger initial water depth led to a more significant reduction rate and
315 also a more intense fluctuation in the water level. As shown in Fig. 5b, the water depth downstream
316 of the gate dramatically increased at first, with the water level being characterized by a continuous
317 decreasing trend after reaching its maximum value. The maximum water levels for the three different
318 initial water depths were 15.0, 12.7, 4.4 cm, respectively. A rapid rise in water depth was recorded at
319 P3 due to the reflection effect of the building.

320 **Insert Fig. 5**

321 Fig. 6 illustrates the processes of flow collision with the first building for Case 4 and with the
322 initial water depth of 30 cm; this is usually referred to as the flip-thorough process (Lugni et al., 2006).
323 When the dam-break flow reached the front wall of the building, it climbed up as a thin layer (Fig.
324 6c). After a very short time, the thin layer flow collapsed and overturned backwards to rejoin the
325 incoming flow, which produced a hydraulic jump associated with intense mixing of turbulence and
326 air. The hydraulic jump gradually moved upstream, with the dam-break flow intensity reducing (Fig.
327 6e and 6f). It is worth noting that the arrival times of dam-break flows, recorded at the measurement
328 points located in the upper part of the model, were almost the same for the different experimental
329 scenarios. However, the recorded arrival times under different initial water depths varied significantly
330 at the measurement points located in the lower part of the model, and a larger initial water depth
331 produced a higher flood wave speed. At P7, the arrival times of the dam-break waves were 6.99, 8.99,
332 15.74 s, respectively, under the initial water depths of 30, 20, 10 cm.

333 **Insert Fig. 6**

334 Theoretically, the velocity and kinetic energy of dam-break flows are associated with the initial
335 water depth. In order to reveal the relationship between the initial water depth and flood intensity,

336 flow velocity measurements were performed during the experiments. As the water depths on the left
337 and right sides of the flume were too shallow to conduct continuous measurements, especially under
338 small initial water depth scenarios, only the flow velocities along the flume centerline were measured.
339 Fig. 7 shows the velocity variations at points P2, P5 and P7 located from upstream to downstream. In
340 general, a larger initial water depth led to a higher flow velocity, especially in the lower part of the
341 idealized street. As shown in Fig. 7a and 7c, the maximum velocities at the upstream side under all
342 scenarios were 1.34, 1.62, 1.78 m/s, respectively, whereas the corresponding velocities at the end of
343 the street were 0.38, 1.35, 1.60 m/s. Furthermore, another noticeable difference is that for the cases
344 with small initial water depths, the maximum velocities of the dam-break flows decreased along the
345 street. However, under the condition of a 30 cm initial water depth, the flow velocity first increased
346 along the model road and then decreased. The maximum velocity at the three measurement points
347 mentioned above was 2.11 m/s, which was located in the middle part of the street.

348 **Insert Fig. 7**

349 **3.3 Flood inundation characteristics for different street layouts**

350 For the case of a 30 cm initial water depth, comparisons of the water depth variations were
351 undertaken for different street layouts. As shown in Fig. 8, there was no apparent difference in the
352 water depth variations at P2 during the first 30 seconds. The reason for this is that the large difference
353 between the water levels at the upstream and downstream locations led to a large flow velocity, as
354 well as supercritical flow conditions. The flow velocity reduced with the decreasing upstream water
355 depth, and the flow pattern was gradually transformed from a supercritical to subcritical state.
356 Therefore, the sudden rise in the water level was recorded at P2, due to the occurrence of the hydraulic
357 jump. As compared with those cases without buildings, the water depth at P3 was much higher, due
358 to the effect of the building reflection. Fig. 8d highlights that the maximum water levels for different

359 scenarios were almost the same at the downstream side of the first building. However, the flood peak
360 time for Case 4 was delayed, reflecting the resistance effect of the urban greenbelts. Furthermore,
361 buildings reduced the wetted cross-sectional area of the street, causing higher water depths on the
362 model road. In conclusion, buildings caused the onset of hydraulic jumps and an increase in the water
363 levels, therefore intensifying the impact of urban flooding disasters. However, the influences of the
364 street layouts and greenbelt areas on the inundation processes of urban floods are relatively
365 insignificant, and the flood inundation process over an urban street is mainly controlled by the
366 upstream boundary condition for this situation.

367 **Insert Fig. 8**

368 **3.4 Mitigation effect of the drainage system on the flood inundation process**

369 In these experiments, all the street inlets were fully submerged in the first 60 seconds after the
370 wet/dry interface reached its location. During this period, the drainage boxes, as well as the side tubes,
371 were converted into a pressurised state, while the main drainage pipe was kept ventilated. Hence, the
372 exchange discharge through the street inlets was related to the water head difference between the
373 surface runoff and the pipe flow. In order to measure the drainage discharge through the street inlets,
374 an electromagnetic flowmeter was located on each side tube. However, accurate measurements of the
375 drainage discharge through the street inlets were challenging for such a highly unsteady flow
376 condition. In the first few seconds, the intense air mixing in rain boxes led to complex two-phase flow
377 patterns in the side tubes, which reduced the accuracy of the discharge hydrographs measured using
378 the flowmeters. Furthermore, the discharge hydrographs measured through the side tubes were
379 significantly delayed relative to the actual discharge processes through the street inlets. Therefore, in
380 addition to the variation in the drainage discharge, the occurrence time when the flow regime in the
381 side tubes converted from ventilated to pressurised was also recorded, to provide the start time of the

382 effective discharge measurement. The average drainage discharges for Cases 5 and 6 over the initial
383 40 s period through inlet1 are presented in Table 3, with these results providing an approximate
384 assessment basis for the model accuracy.

385 Fig. 9 illustrates the influence of the drainage system on the variation in the surface water depth.
386 As most of the street inlets were located at the middle and lower sides of the street, the reduction in
387 the water depth became more apparent from the upper to the lower part of the flume. The sewer
388 system not only reduced the surface water depth, but also had a significant influence on the velocity
389 of the dam break flow. The flow depths at P7 were 1.81 cm and 2.17 cm, respectively, under scenarios
390 with and without the drainage system after the gate opening of 40 seconds, with the corresponding
391 wave arrival times of 16.21 s and 14.75 s respectively. In conclusion, street inlets were found to
392 reduce both the water depth and flood wave velocity, which significantly shortened the flood
393 inundation time.

394 **Insert Fig. 9**

395 **Insert Table 3**

396 **3.5 Comparisons between numerical simulations and experimental observations**

397 Fig. 10 illustrates a comparison of the simulated and experimentally observed variations in the
398 water depth hydrographs at different measurement points for Case 2. In general, the SWEs model
399 used in this study has accurately reproduced the water level variations throughout the whole process,
400 with relative errors of less than 5% at most of the measurement points. However, there were some
401 visible differences between the simulated results and the observed data at the measurement points P2
402 and P3, and the simulated flood peak levels were noticeably lower than the observed values, with the
403 relative errors being 5.46% and 35.7%, respectively (Fig. 10b and 10c). At these locations, the dam-
404 break flow was characterized by pronounced three-dimensional properties, which cannot be described

405 by the traditional 2D SWEs. When the dam-break wave impinged on these buildings, the collision
406 between the reflection wave and the incoming flow caused violent turbulence and air entertainment,
407 and the current SWEs model is not capable of predicting such complex 3D flow patterns. Furthermore,
408 it should be noted that the free-surface oscillations were not successfully reproduced, and the
409 simulated water level hydrograph was smoother than the observed one. In addition to water depth
410 variations, the model results show some errors in capturing the wet/dry front, and the simulated arrival
411 time of the dam-break wave at P6 was delayed relative to the observed value.

412 **Insert Fig. 10**

413 **3.6 Numerical modelling with the inclusion of street inlets**

414 In this section, the discharge data measured using the electromagnetic flowmeters were directly
415 used to provide the drainage discharges through the street inlets. The computational meshes within
416 each street inlet were identified as exchange cells, where the mass source term q_L in Eq. (1) is non-
417 zero. The exchange discharge within a mesh (Q_m) is calculated using the formula:

$$Q_m = \frac{Q_i \times A_m}{A_i} \quad (12)$$

418 where the subscript m represents the index of computation cells; and A_m is the area of the mesh.

419 It should be noted that the influence of a street inlet in previous studies reported in the literature
420 (Bazin et al., 2014; Noh et al., 2016; Rubinato et al., 2017) is usually represented by a mass source
421 point, through which the surface runoff is added (or subtracted) to the underground sewer flow.
422 However, street inlets not only affect the mass term but also directly influence the momentum balance
423 of the surface runoff. Many researchers have investigated the flow velocity fields, turbulence
424 characteristics, and local energy losses in manholes and sewer junctions (Rubinato et al., 2018; Kim
425 et al., 2018). However, investigations into the influence of a sewer system on the surface runoff are
426 seldom reported. Further investigations into the local energy loss and velocity field variations caused

427 by street inlets should be carried out in the future to improve the predictive accuracy of the numerical
428 model. The temporal evolutions of the velocity field and water level distribution around a street inlet
429 are illustrated in Fig. 11. After the gate opening of 3 seconds, the wet/dry interface reached the
430 location of the first street inlet. During the first 20 seconds, the positions of the maximum velocity
431 and minimum water depth within a street inlet were located at the downstream side, due to the high
432 velocity of the dam-break flow (Fig. 11 a-d). As the velocity of the dam-break flow decreased, the
433 positions of the maximum flow velocity and minimum water depth gradually moved upstream (Fig.
434 11e, f). The water level around a street inlet was significantly lower than the value in the adjacent
435 area, and street inlets also influenced the local velocity fields, with the velocity vector in the adjacent
436 area pointing slightly towards the centerline of the street inlet.

437 **Insert Fig. 11**

438 **4 Discussion**

439 **4.1 Effect of mesh resolution**

440 Mesh generation and resolution are critical in terms of acquiring accurate numerical predictions
441 in computational model studies. Variations in the mesh resolution can lead to different simulated
442 results and computational requirements. A finer mesh resolution benefits the representation of a
443 computational domain, particularly for complex bathymetries and solid structures etc., and also
444 provides more accurate predictions of small-scale hydraulic features. However, the use of small
445 meshes also reduces the computational efficiency in terms of increasing the mesh amount and
446 shortening the numerical time step (Horritt et al., 2006). In the current study, indicators such as the
447 Nash-Sutcliffe efficiency (NSE) and the root mean square error (RMSE) are used to evaluate the
448 model performance using different mesh resolutions. The Nash-Sutcliffe efficiency coefficient (NSE)
449 is one of the most frequently used evaluation criterion in hydrodynamic modeling and is given by:

$$\text{NSE} = 1 - \frac{\sum_{i=1}^{AMT} (y_i - \hat{y}_i)^2}{\sum_{i=1}^{AMT} (y_i - \bar{y})^2} \quad (13)$$

450 where AMT is the amount of data points; y_i is the observed value (in this section y is the water depth);
 451 \hat{y}_i is the simulated value; and \bar{y} is the average value of the observed data.

452 The root mean square error (RMSE) is another widely used criterion, which provides a valuable
 453 general-purpose error metric parameter for comparing numerical model predictions and is given by:

$$\text{RMSE} = \sqrt{\frac{1}{AMT} \sum_{i=1}^{AMT} (y_i - \hat{y}_i)^2} \quad (14)$$

454 In order to assess the relationship between the mesh resolution and computational results,
 455 numerical simulations were conducted using meshes with resolutions of 5, 10, and 20 cm. Fig. 12
 456 illustrates the variations in the NSE and RMSE parameters for the different mesh resolutions.

457 Generally, the numerical model accurately reproduced the water level variations at most of the
 458 measurement points, with the NSE values being greater than 0.9 and the RMSE values less than $1 \times$
 459 10^{-3} . As expected, the results using the 5 cm mesh resolution gives the best performance. In addition,
 460 the model-performance difference between the mesh sizes of 5 cm and 10 cm is smaller than the
 461 difference between the mesh sizes of 10 cm and 20 cm, suggesting that further refinement of the
 462 computational mesh would only slightly improve the computational results. The model performance
 463 evaluation discussed above was also conducted for different initial water depths, and it was clear that
 464 as comparison with the larger initial water depth scenarios, the small initial water depth scenarios
 465 were more sensitive to the mesh resolution. Furthermore, the computational times differ significantly
 466 between the different mesh resolutions. The mesh resolutions of 5, 10, and 20 cm corresponded to
 467 52516, 13684, 3440 cells, respectively, and led to the corresponding computational times of 22, 8,
 468 and 2 minutes. Based on the above analysis, it was deemed necessary to select the appropriate mesh
 469 size to balance the computational efficiency with accuracy in the numerical modelling.

470 **Insert Fig. 12**

471 **4.2 Comparison of different discharge capacity formulae in the numerical model**

472 Street inlets control the interaction between surface runoff and underground pipe flow, and

473 therefore, these inlets directly affect the extent of urban flood inundation. The calculation of drainage
474 discharge through street inlets is one of the most critical factors in simulating urban flooding. Most
475 of the existing discharge capacity formulae for street inlets are derived from laboratory experiments
476 under steady-state flow conditions. In order to test the applicability of these formulae in simulating
477 highly unsteady urban flood events, different discharge capacity formulae for street inlets were
478 integrated into the 2D SWEs model based on the finite volume method, and the integrated model was
479 used to reproduce the flood inundation processes, as well as the flow exchange through the street
480 inlets. In this study only the following formulations were selected for comparison and evaluation in
481 the model studies, including: (i) the weir and orifice formulae, which considered the influence of the
482 rain box, termed as WOFR (i.e. Eqs. (7) - (9)); (ii) the simplified weir and orifice formulae, termed
483 as SWOF, which only included the discharge capacity of the inlet grates (i.e. Eq. (7)); and (iii) the
484 unified discharge capacity formula, termed as UF (i.e. Eq. (10)). The key parameters in these
485 discharge capacity formulae were governed by many factors, such as the shape and void ratio of the
486 inlet grates, the size of the rain boxes, and also the geometry of side tubes. Therefore, parameter
487 calibration was essential in the absence of a generally accepted standard for the discharge coefficients
488 for different types of inlets. In this study, the coefficients were calibrated using the trial and error
489 method based on numerical tests, and the calibrated values are presented in Fig. 13a. For the weir and
490 orifice formulae, many researchers have suggested to use the ratio of the total surface water head to
491 the thickness of inlet grate, as the criteria to distinguish the weir and orifice drainage status (Chanson
492 et al., 2002; Noh et al., 2016). Based on experimental observations, as well as numerical simulations,
493 $h_{ii}/w = 0.2$ was used as the criterion to distinguish the weir and orifice flows, where w is the width of
494 the inlet grate.

495 Fig. 13 presents the results using different discharge capacity formulae. As shown in Fig. 13a,

496 the SWEs model, including different discharge capacity formulae, can accurately reproduce the water
497 level variation with careful calibration of the model parameters. About 0.23 m³ of the surface runoff
498 was drained through the street inlets in the first 40 seconds, accounting for as much as 17% of the
499 total flow volume. The simulated discharge hydrographs drained through inlet5, using different
500 discharge capacity formulae, are shown in Fig. 13b. The results obtained using the WOFR showed a
501 significant difference as comparison with the results obtained using the SWOF and UF. In the first
502 few seconds, the rain box was ventilated, and the street inlet showed a larger drainage efficiency.
503 After the rain box was pressurised, the drainage efficiency was mainly determined by the discharge
504 capacity of the side tube, and the drainage discharge was relatively small. This phenomenon agreed
505 well with the fact that the discharge capacity for the inlet grate was larger than the capacity of the
506 side tube. The drainage discharge difference was 1.4 L/s between the cases for the ventilated and
507 pressurised rain boxes, indicating a high sensitivity to the conversion of the hydraulic status within
508 the rain box. The results from the UF and SWOF showed similar characteristics. The drainage
509 discharge gradually reduced after reaching the maximum value, which was 0.80 and 0.82 L/s,
510 respectively. As the SWOF lacks inclusion of the influence of the side tubes, parameter modifications
511 were required to provide an indirect reflection. The calibrated inlet orifice coefficient w_{is} was set to
512 0.12 for the WOFR, while the value was set to 0.03 for the SWOF.

513 The simulated drainage discharges through the different street inlets for the WOFR and UF are
514 presented in Figs. 13c and 13d, respectively. According to the structure of the UF, the exchange
515 discharge is directly related to the surface water depth and the flow velocity, which decreases along
516 the street. Therefore, the street inlets located at the upstream side of the flume had a larger drainage
517 efficiency than the other street inlets. However, for the WOFR, the discharge capacity of a street inlet
518 was determined by the water head difference between the surface runoff and the underground sewer

519 flow after the rain box was pressurised. As the water head of surface runoff was relatively small
520 compared to the height between the main pipe and the road surface, the drainage efficiency varied
521 slightly from the upper and lower part of the flume.

522 In general, the integrated model can accurately simulate the variation in the surface water depth
523 when the impacts of street inlets and sewer pipes are included. However, the weir and orifice formulae
524 provide flexibility in terms of characterizing the structures and physical processes of different sewer
525 systems and are more capable of capturing the transition of the inlet drainage status. However, the
526 UF and SWOF lack consideration of some critical physical processes. Therefore, modifications of the
527 empirical parameters are required to provide an approximate solution. This approximation is
528 challenging to meet the actual requirements for accurate predictions and may therefore introduce
529 some additional uncertainties in the numerical model predictions.

530 **Insert Fig. 13**

531 **5 Conclusions**

532 In the current study, an idealized laboratory model of a typical urban street with a sewer system
533 underneath, was set-up to acquire a better understanding of the flood inundation processes occurring
534 in an urban environment. In order to reflect the influence of different street layouts and infrastructures
535 on the flood processes, detailed water level evolutions and flow velocity variations were measured at
536 several predetermined points for different experimental scenarios. In addition to the detailed flume
537 experiments, numerical model simulations were also conducted using a 2D SWEs model, with
538 different discharge capacity formulae for street inlets being included in the model, in order to replicate
539 the flood inundation processes and the interaction between the surface runoff and sewer system
540 discharge. The conclusions from the laboratory experiments and the numerical model simulations can
541 be summarised as follows:

542 (i) Based on the analysis of the experimental results, it was found that buildings would reduce the
543 wetted cross-sectional area of flow and therefore increase the water levels on the road. Compared
544 with the street layout, the upstream boundary condition and the sewer system capacity have a more
545 significant influence on the highly unsteady urban flood inundation processes. A larger building
546 density and the arrangement of greenbelt areas can slightly increase the water depth on the road. The
547 use of urban sewer systems can reduce both the water depth and the flow velocity and, therefore,
548 effectively alleviate the disaster of urban flooding and waterlogging.

549 (ii) The 2D SWEs model used in this study was shown to be capable of simulating the urban flood
550 inundation processes, with the NSE values being larger than 0.9 and the RMSE values being less than
551 0.15×10^{-3} at all the measurement points. Based on the simulated results, it was found that for a 10 cm
552 initial water depth, about 17% of the total volume was drained from the surface to the sewer system
553 during the first 40 seconds. The street inlets not only reduced the runoff water depth, but also changed
554 the local velocity field, and the position of the maximum velocity and minimum water depth around
555 a street inlet, with these parameters varying with the incoming flow intensity.

556 (iii) A sensitive analysis indicated that a fine resolution mesh improved the model performance,
557 in terms of accuracy. However, further refinements to the mesh were only slight, but the numerical
558 model simulations led to much more computational time being required after reaching a certain mesh
559 resolution. This meant that real-time, long-term and large-scale simulations were unrealistic.
560 Furthermore, the choice of the discharge capacity formulae for representing street inlets plays an
561 essential role in improving the accuracy of dual drainage modeling. The weir and orifice formulae,
562 with the inclusion of the impact of the rain box, were more accurate in capturing the transition of the
563 drainage discharge through street inlets and showed the best performance in this study.

564

565 **Acknowledgments**

566 This work was funded by the National Natural Science Foundation of China (Grant Nos. 51725902,
567 41890820); the Royal Academy of Engineering through the Urban Flooding Research Policy Impact
568 Programme (Grant No. UFRIP\100031); and the Newton Advanced Fellowships from the NSFC
569 and the UK Royal Society (Grant Nos. 52061130219; NAF\R1\201156).

570

571 **References**

572

- 573 [1] Aureli, F., Dazzi, S., Maranzoni, A., Mignosa, P. and Vacondio, R., 2015. Experimental and numerical evaluation
574 of the force due to the impact of a dam-break wave on a structure. *Advances in Water Resources*, 76: 29-42.
- 575 [2] Bazin, P., Nakagawa, H., Kawaike, K., Paquier, A. and Mignot, E., 2014. Modeling flow exchanges between a street
576 and an underground drainage pipe during urban floods. *Journal of Hydraulic Engineering*, 140: 04014051.
- 577 [3] Bennett, N.D. et al., 2013. Characterising performance of environmental models. *Environmental Modelling &*
578 *Software*, 40(2013): 1-20.
- 579 [4] Chanson, H., Aoki, S. and Maruyama, M., 2002. Unsteady two-dimensional orifice flow: a large-size experimental
580 investigation. *Journal of Hydraulic Research*, 40(1): 63-71.
- 581 [5] Chen, B., Krajewski, W.F., Goska, R. and Young, N., 2017. Using LiDAR surveys to document floods: A case study
582 of the 2008 Iowa flood. *Journal of Hydrology*, 553: 338-349.
- 583 [6] Chen, Q., Xia JQ., Dong B., 2020. Experimental study on discharge capacity of street inlet in urban flooding.
584 *Advances in Water Science*, 2020,31(01):10-17. (In Chinese) doi: 10.14042/j.cnki.32.1309.2020.01.002
- 585 [7] Chen, S. et al., 2018. Variance based sensitivity analysis of 1D and 2D hydraulic models: An experimental urban
586 flood case. *Environmental Modelling & Software*, 109: 167-181.
- 587 [8] Cheng, X., Han, G., Zhao, Y. and Li, L., 2019. Evaluating Social Media Response to Urban Flood Disaster: Case
588 Study on an East Asian City (Wuhan, China). *Sustainability*, 11(19): 5330. doi: 10.3390/su11195330.
- 589 [9] Ferreira, C.S.S. et al., 2019. Impacts of distinct spatial arrangements of impervious surfaces on runoff and sediment
590 fluxes from laboratory experiments. *Anthropocene*, 28(2019): 100219.
- 591 [10] Fraga, I., Cea, L. and Puertas, J., 2017. Validation of a 1D-2D dual drainage model under unsteady part-full and
592 surcharged sewer conditions. *Urban Water Journal*, 14(1): 74-84.
- 593 [11] Ghostine, R. et al., 2009. Simulation of supercritical flow in crossroads: Confrontation of a 2D and 3D numerical
594 approaches to experimental results. *Computers & Fluids*, 38(2): 425-432.
- 595 [12] Gómez, M. and Russo, B., 2011. Methodology to estimate hydraulic efficiency of drain inlets. *Proceedings of the*
596 *Institution of Civil Engineers - Water Management*, 164(2): 81-90.
- 597 [13] Gómez, M., Rabasseda, G.H. and Russo, B., 2013. Experimental campaign to determine grated inlet clogging factors

- 598 in an urban catchment of Barcelona. *Urban Water Journal*, 10(1): 50-61.
- 599 [14] Horritt, M.S., Bates, P.D. and Mattinson, M.J., 2006. Effects of mesh resolution and topographic representation in
600 2D finite volume models of shallow water fluvial flow. *Journal of Hydrology*, 329(1-2): 306-314.
- 601 [15] Jang, J., Chang, T. and Chen, W., 2018. Effect of inlet modelling on surface drainage in coupled urban flood
602 simulation. *Journal of Hydrology*, 562: 168-180.
- 603 [16] Kim, J., Jo, J. and Yoon, S., 2018. Head Loss Reduction in Surcharged Four-Way Junction Manholes. *Water*, 10(12):
604 1741. doi: 10.3390/w10121741
- 605 [17] LaRocque, L.A., Elkholy, M., Hanif Chaudhry, M. and Imran, J., 2013. Experiments on Urban Flooding Caused by
606 a Levee Breach. *Journal of Hydraulic Engineering*, 139(9): 960-973.
- 607 [18] Lauber, G. and Hager, W.H., 1998. Experiments to dambreak wave: Horizontal channel. *Journal of Hydraulic
608 Research*, 36(3): 291-307.
- 609 [19] Leandro, J., Chen, A.S., Djordjević, S. and Savić, D.A., 2009. Comparison of 1D/1D and 1D/2D Coupled
610 (Sewer/Surface) Hydraulic Models for Urban Flood Simulation. *Journal of Hydraulic Engineering*, 135(6): 495-504.
- 611 [20] Lee, S., Nakagawa, H., Kawaike, K. and Zhang, H., 2012. Study on Inlet Discharge Coefficient Through the
612 Different Shapes of Storm Drains for Urban Inundation Analysis. *Journal of Japan Society of Civil Engineers*, 68(4):
613 I_31-I_36.
- 614 [21] Lee, S., Nakagawa, H., Kawaike, K. and Zhang, H., 2016. Urban inundation simulation considering road network
615 and building configurations. *Journal of Flood Risk Management*, 9(3): 224-233.
- 616 [22] Li, Q., Liang, Q. and Xia, X., 2020. A novel 1D-2D coupled model for hydrodynamic simulation of flows in drainage
617 networks. *Advances in Water Resources*, 137: 103519.
- 618 [23] Li, Z. et al., 2019. Comparative Analysis of Building Representations in TELEMAC-2D for Flood Inundation in
619 Idealized Urban Districts. *WATER*, 11(9): 1840. doi: 10.3390/w11091840
- 620 [24] Lugni, C., Brocchini, M. and Faltinsen, O.M., 2006. Wave impact loads: The role of the flip-through. *Physics of
621 Fluids*, 18(12): 122101.
- 622 [25] Martínez-Aranda, S., Fernández-Pato, J., Caviedes-Voullième, D., García-Palacín, I. and García-Navarro, P., 2018.
623 Towards transient experimental water surfaces: A new benchmark dataset for 2D shallow water solvers. *Advances
624 in Water Resources*, 121: 130-149.
- 625 [26] Martins, R. et al., 2018. On the Characteristics of Velocities Fields in the Vicinity of Manhole Inlet Grates During
626 Flood Events. *Water Resources Research*, 54(9): 6408-6422.
- 627 [27] Mignot, E. et al., 2013. Impact of topographic obstacles on the discharge distribution in open-channel bifurcations.
628 *Journal of Hydrology*, 494: 10-19.
- 629 [28] Mignot, E., Li, X. and Dewals, B., 2019. Experimental modelling of urban flooding: A review. *Journal of Hydrology*,
630 568: 334-342.
- 631 [29] Mignot, E., Paquier, A. and Haider, S., 2006. Modeling floods in a dense urban area using 2D shallow water
632 equations. *Journal of Hydrology*, 327(1-2): 186-199.
- 633 [30] Naves, J., Anta, J., Suárez, J. and Puertas, J., 2020. Hydraulic, wash-off and sediment transport experiments in a
634 full-scale urban drainage physical model. *Scientific Data*. doi:10.1038/s41597-020-0384-z .

- 635 [31] Noh, S.J., Lee, S., An, H., Kawaike, K. and Nakagawa, H., 2016. Ensemble urban flood simulation in comparison
636 with laboratory-scale experiments: Impact of interaction models for manhole, sewer pipe, and surface flow.
637 *Advances in Water Resources*, 97: 25-37.
- 638 [32] Puech, C. and Raclot, D., 2002. Using geographical information systems and aerial photographs to determine water
639 levels during floods. *Hydrological Processes*, 16(8): 1593-1602.
- 640 [33] Qian, C., Junqiang, X. and Boliang, D., 2020. Experimental study on discharge capacity of street inlet in urban
641 flooding. *Advances in Water Science*, 31(1): 10-17.
- 642 [34] Rubinato, M. et al., 2017. Experimental calibration and validation of sewer/surface flow exchange equations in
643 steady and unsteady flow conditions. *Journal of Hydrology*, 552: 421-432.
- 644 [35] Rubinato, M., Lee, S., Martins, R. and Shucksmith, J.D., 2018. Surface to sewer flow exchange through circular
645 inlets during urban flood conditions. *Journal of Hydroinformatics*, 20(3): 564-576.
- 646 [36] Sanders, B.F. and Bradford, S.F., 2011. Network Implementation of the Two-Component Pressure Approach for
647 Transient Flow in Storm Sewers. *Journal of Hydraulic Engineering*, 137(2): 158-172.
- 648 [37] Seyoum, S.D., Vojinovic, Z., Price, R.K. and Weesakul, S., 2012. Coupled 1D and Noninertia 2D Flood Inundation
649 Model for Simulation of Urban Flooding. *Journal of Hydraulic Engineering*, 138(1): 23-34.
- 650 [38] Shao, Z., Fu, H., Li, D., Altan, O. and Cheng, T., 2019. Remote sensing monitoring of multi-scale watersheds
651 impermeability for urban hydrological evaluation. *Remote Sensing of Environment*, 232(2019): 111338.
- 652 [39] Soares-Frazão, S. and Zech, Y., 2007. Experimental study of dam-break flow against an isolated obstacle. *Journal*
653 *of Hydraulic Research: Dam-Break Flow Experiments and Real-Case Data. A Database from the European IMPACT*
654 *Research Program*, 45(sup1): 27-36.
- 655 [40] Soares-Frazão, S. and Zech, Y., 2008. Dam-break flow through an idealised city. *Journal of Hydraulic Research*,
656 46(5): 648-658.
- 657 [41] Testa, G., Zuccalà, D., Alcrudo, F., Mulet, J. and Soares-Frazão, S., 2007. Flash flood flow experiment in a
658 simplified urban district. *Journal of Hydraulic Research: Dam-Break Flow Experiments and Real-Case Data. A*
659 *Database from the European IMPACT Research Program*, 45(sup1): 37-44.
- 660 [42] van Leer, B., 1979. Towards the ultimate conservative difference scheme. V. A second-order sequel to Godunov's
661 method. *Journal of Computational Physics*, 32(1): 101-136.
- 662 [43] Vasconcelos, J.G., Wright, S.J. and Roe, P.L., 2006. Improved Simulation of Flow Regime Transition in Sewers:
663 Two-Component Pressure Approach. *Journal of Hydraulic Engineering*, 132(6): 553-562.
- 664 [44] von Hafen, H., Goseberg, N., Stolle, J. and Nistor, I., 2019. Gate-Opening Criteria for Generating Dam-Break Waves.
665 *Journal of Hydraulic Engineering*, 145(3): 04019002.
- 666 [45] Xia, J., Falconer, R.A., Lin, B. and Tan, G., 2011. Numerical assessment of flood hazard risk to people and vehicles
667 in flash floods. *Environmental Modelling & Software*, 26(8): 987-998.

668

669 **List of Table and Figure Captions**

670 **Table 1** Positions of water level gauges and buildings.

671 **Table 2** Summary of experimental runs and corresponding conditions.

672 **Table 3** Averaged drainage discharges through inlet1 for different cases. (Unit: L/s)

673
674
675
676
677
678
679
680
681
682
683
684
685
686
687
688
689
690
691
692
693
694
695
696
697
698
699
700
701
702
703
704
705
706
707
708
709
710

711 **Fig. 1** Sketch of the physical model showing a typical urban street.

712 **Fig. 2** Sketch of the drainage status between surface runoff and sewer pipe flow.

713 **Fig. 3** Zoom of the mesh characterization around a street inlet.

714 **Fig. 4** Spatial and temporal evolutions of the dam-break flow for Case 2 at different times of: (a) $t=$
715 1.0 s; (b) $t=2.0$ s; (c) $t=4.0$ s; (d) $t=6.0$ s; (e) $t=8.0$ s; (f) $t=10.0$ s.

716 **Fig. 5** Temporal variations in water depth at sites of: (a) P1; (b) P2; (c) P3; (d) P4; (e) P5; (f) P7.

717 **Fig. 6** Video images showing the process of the collision between the dam-break flow and the
718 building for Case 4, for an initial water depth of 30 cm at different times of: (a) $t=0.00$ s; (b) $t=1.73$
719 s; (c) $t=2.10$ s; (d) $t=2.83$ s; (e) $t=3.29$ s; (f) $t=4.79$ s.

720 **Fig. 7** Temporal variations in flow velocities for different initial water depths at sites of: (a) P2; (b)
721 P5; (c) P7.

722 **Fig. 8** Comparisons of water depth hydrographs for various street layouts at sites of: (a) P1; (b) P2;
723 (c) P3; (d) P4; (e) P5; (f) P7.

724 **Fig. 9** Effects of the sewer system on water depth variations for the initial water depth of 10 cm
725 (Cases 4 and 6) at sites of: (a) P1; (b) P2; (c) P3; (d) P4; (e) P5; (f) P7.

726 **Fig. 10** Comparisons between simulated and observed variations in the water depth hydrographs at
727 sites of: (a) P1; (b) P2; (c) P3; (d) P4; (e) P5; (f) P6.

728 **Fig. 11** Velocity fields and water level distributions around the first street inlet for Case 2, for a 30
729 cm initial water depth at different times of: (a) $t=3$ s; (b) $t=6$ s; (c) $t=10$ s; (d) $t=20$ s; (e) $t=30$ s; (f)
730 $t=40$ s.

731 **Fig. 12** Model performance variations for different mesh resolutions under initial water depths of:
732 (a) 10 cm; (b) 20 cm; (c) 30 cm.

733 **Fig. 13** Simulated hydrographs of surface water depth, drainage discharge and total drainage volume
734 based on different discharge capacity formulae, showing: (a) surface water depth variations at P5; (b)
735 simulated and measured drainage discharges through inlet5; and (c, d) drainage discharge variations
736 along the street direction and total drainage volume obtained using the WOFR and UF, respectively.

737

738

739

740

741

742

743

744

745

746

747

Table 1 Positions of water level gauges and buildings.

Positions	P1	P2	P3	P4	P5	P6	P7	Building 1	Building 2
x (m)	3.7	4.9	7.0	8.0	9.5	13.5	16.2	7.5	7.5
y (m)	1.5	1.5	0.4	0.5	1.5	1.5	1.5	0.4	2.6

748

749

750

751

752

753

754

755

756

757

758

759

760

Table 2 Summary of experimental runs and corresponding conditions.

Case	Number of buildings	Building spacing(m)	Greenbelt	Sewer system	Initial water depth (cm)
1	×	×	×	×	10/20/30
2	12	0.80	×	×	10/20/30
3	12	0.80	√	×	10/20/30
4	16	0.55	×	×	10/20/30
5	12	0.80	×	√	10/20/30
6	16	0.55	×	√	10/20/30

761

762
763
764
765
766
767
768
769
770
771
772
773
774
775
776
777
778
779
780
781

Table 3 Averaged drainage discharges through inlet1 for different cases. (Unit: L/s)

Q_i	30 cm	20 cm	10 cm
Case 5	0.69	0.68	0.67
Case 6	0.71	0.69	0.68

782

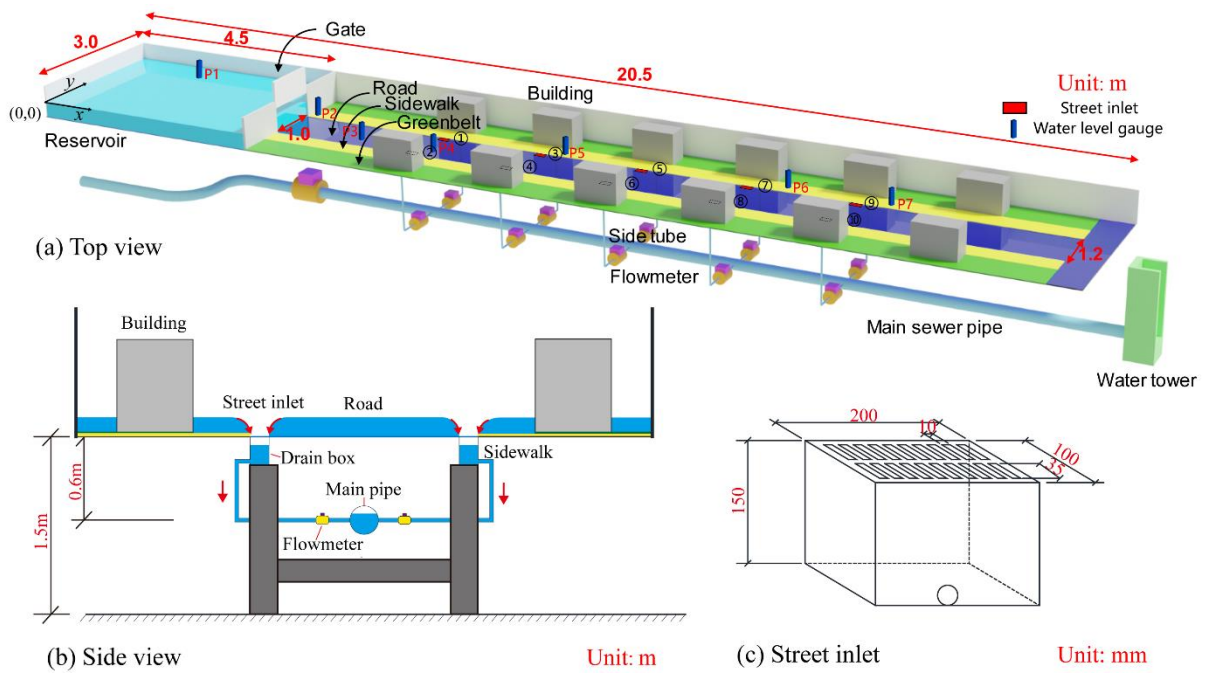
783

784

785

786

787



788

789 **Fig. 1** Sketch of the physical model showing a typical urban street.

790

791

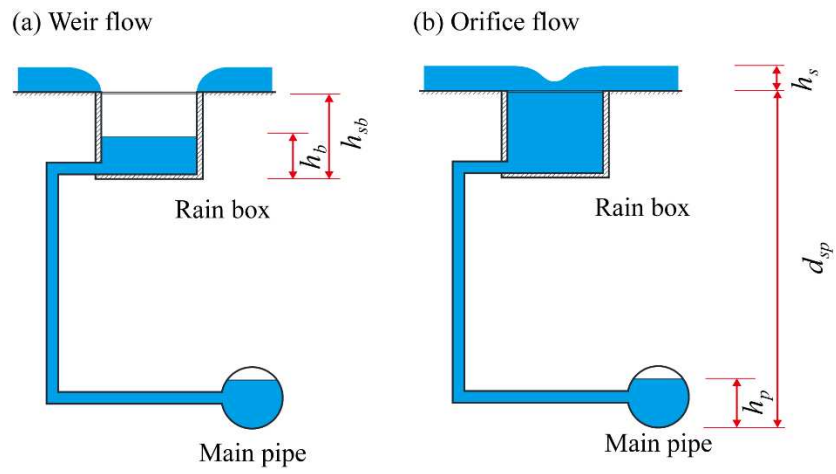
792

793

794

795

796

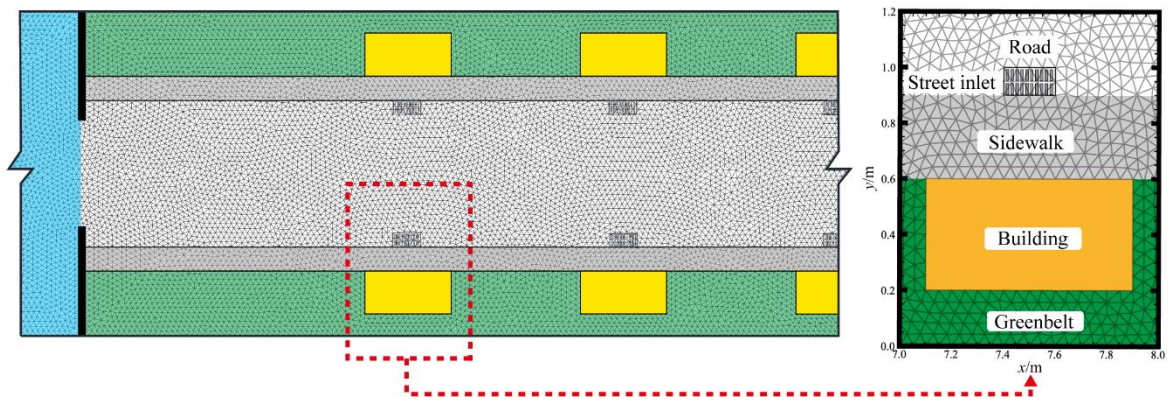


797

798 **Fig.2** Sketch of the drainage status between surface runoff and sewer pipe flow.

799

800
801
802
803
804
805



806
807
808

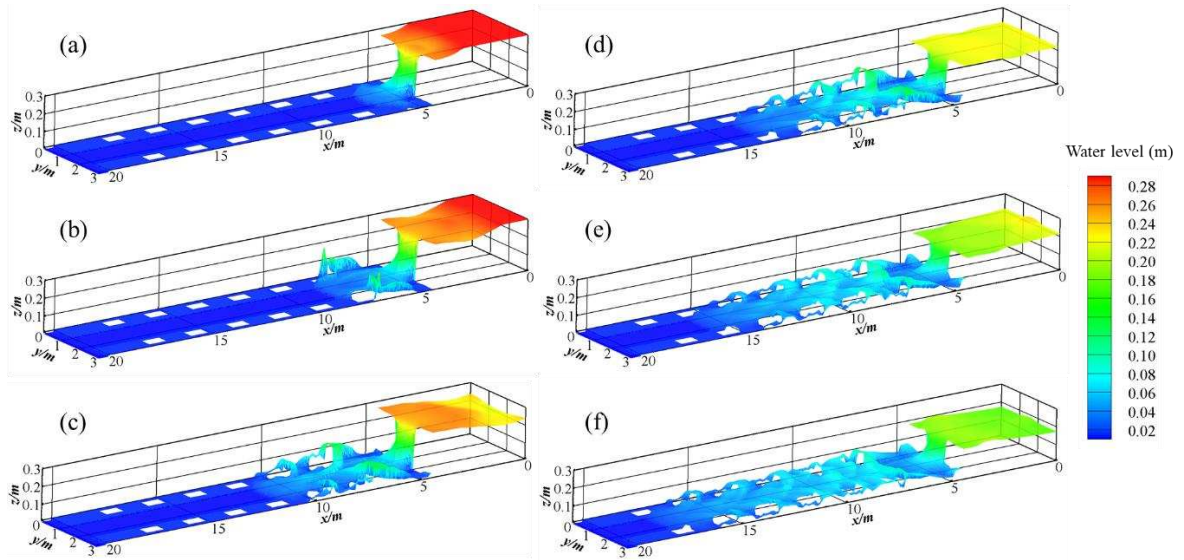
Fig. 3 Zoom of the mesh characterization around a street inlet.

809

810

811

812



813

814 **Fig. 4** Spatial and temporal evolutions of the dam-break flow for Case 2 at different times of: (a) $t=$

815 1.0 s; (b) $t=2.0$ s; (c) $t=4.0$ s; (d) $t=6.0$ s; (e) $t=8.0$ s; (f) $t=10.0$ s.

816

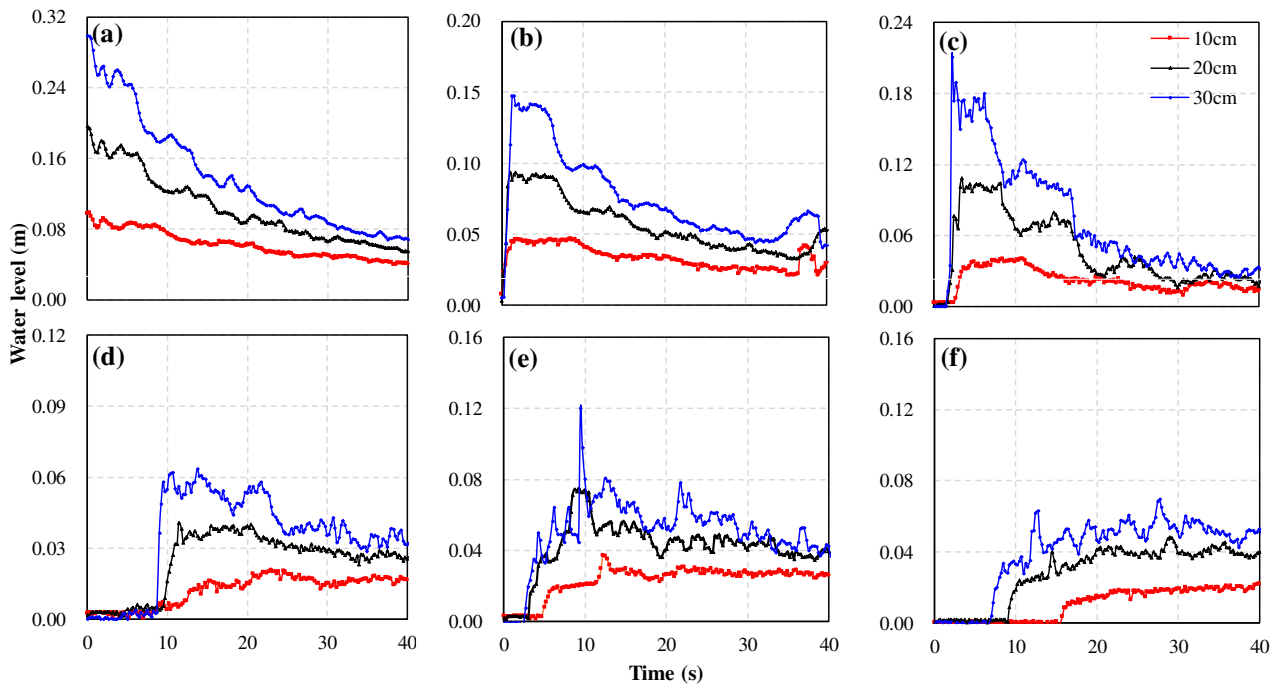
817

818

819

820

821

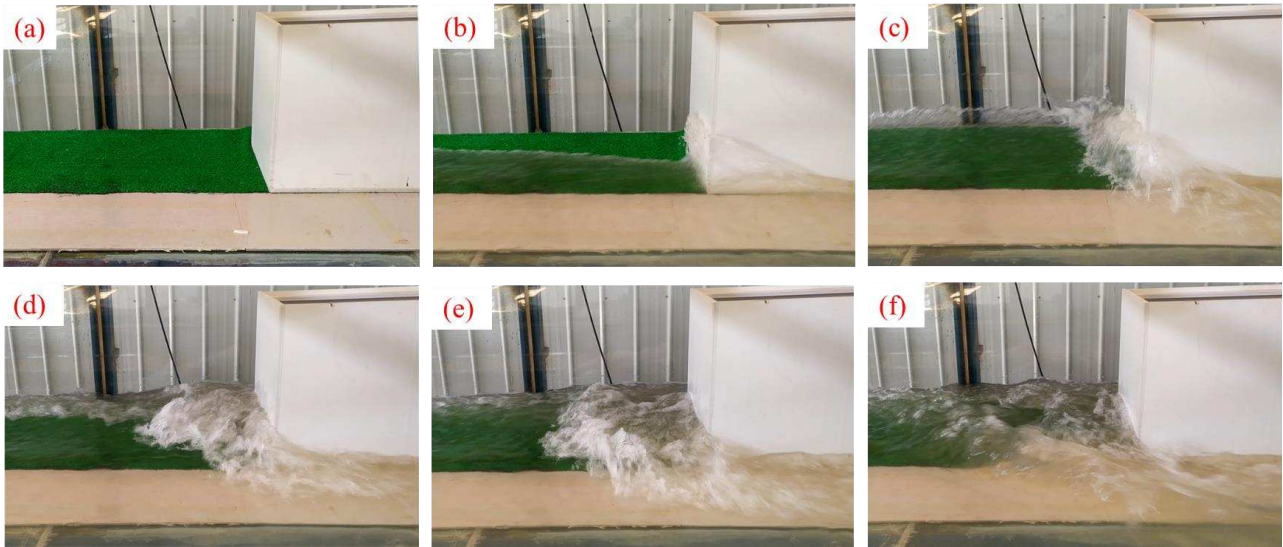


822

823 **Fig. 5** Temporal variations in water depth at sites of: (a) P1; (b) P2; (c) P3; (d) P4; (e) P5; (f) P7.

824

825
826
827
828
829
830
831
832



833

834 **Fig. 6** Video images showing the processes of the collision between the dam-break flow and the
835 building for Case 4, for an initial water depth of 30 cm at different times of: (a) $t=0.00$ s; (b) $t=1.73$
836 s; (c) $t=2.10$ s; (d) $t=2.83$ s; (e) $t=3.29$ s; (f) $t=4.79$ s.

837

838

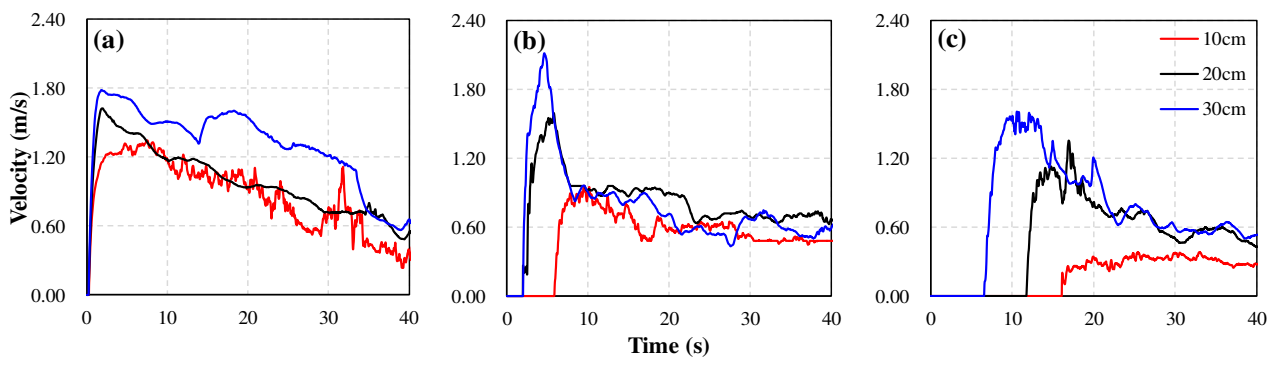
839

840

841

842

843



844

845 **Figure 7** Temporal variations in flow velocities for different initial water depths at sites of: (a) P2;

846 (b) P5; (c) P7.

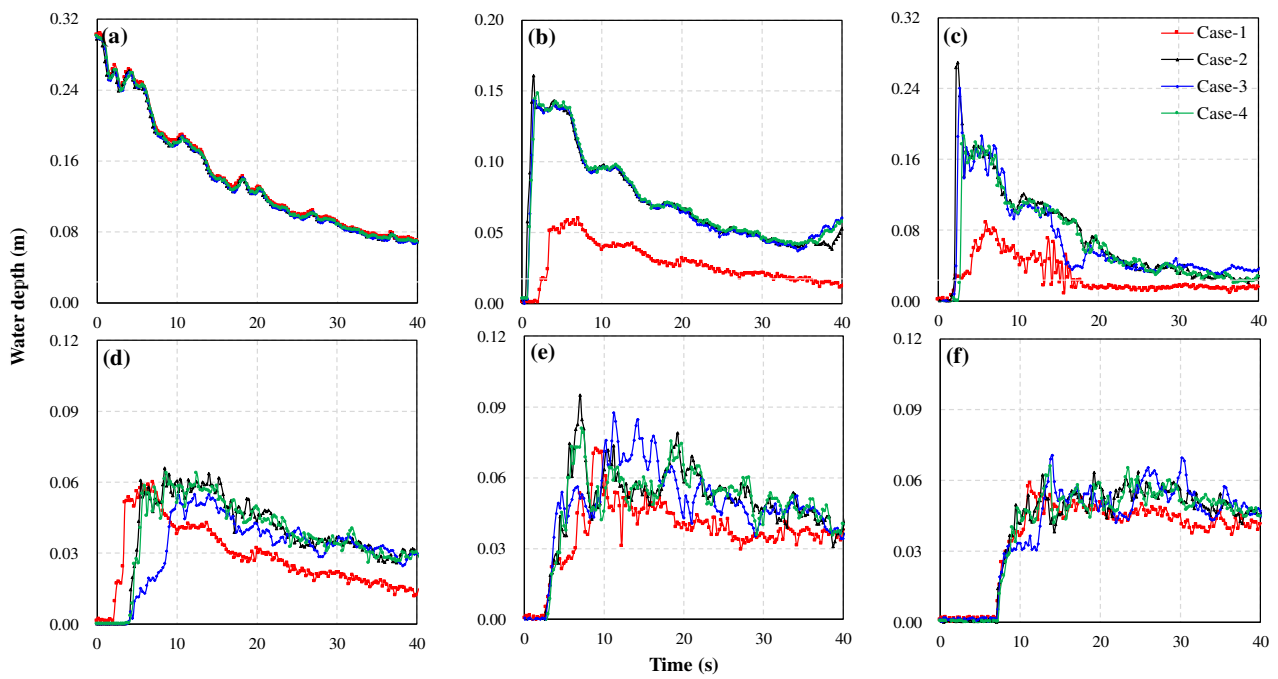
847

848

849

850

851



852

853 **Fig. 8** Comparisons of water depth hydrographs for various street layouts at sites of: (a) P1; (b) P2;

854 (c) P3; (d) P4; (e) P5; (f) P7.

855

856

857

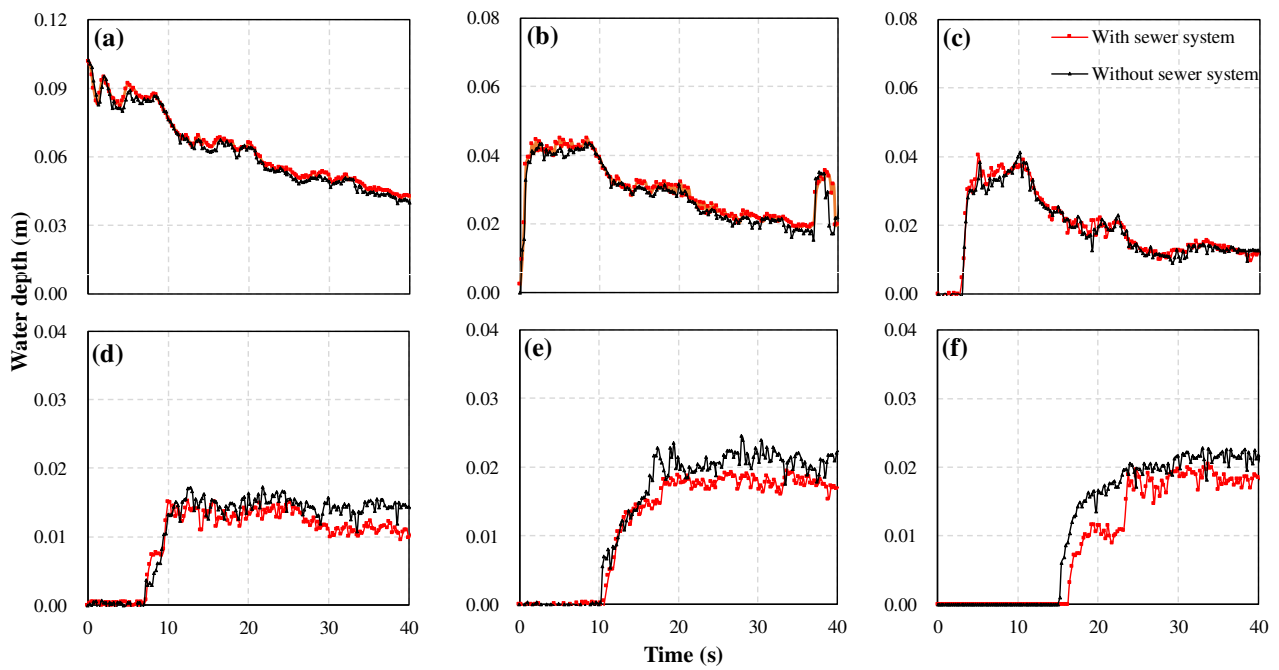
858

859

860

861

862



863

864 **Fig. 9** Effects of the sewer system on water depth variations for the initial water depth of 10 cm

865 (Cases 4 and 6) at sites of: (a) P1; (b) P2; (c) P3; (d) P4; (e) P5; (f) P7.

866

867

868

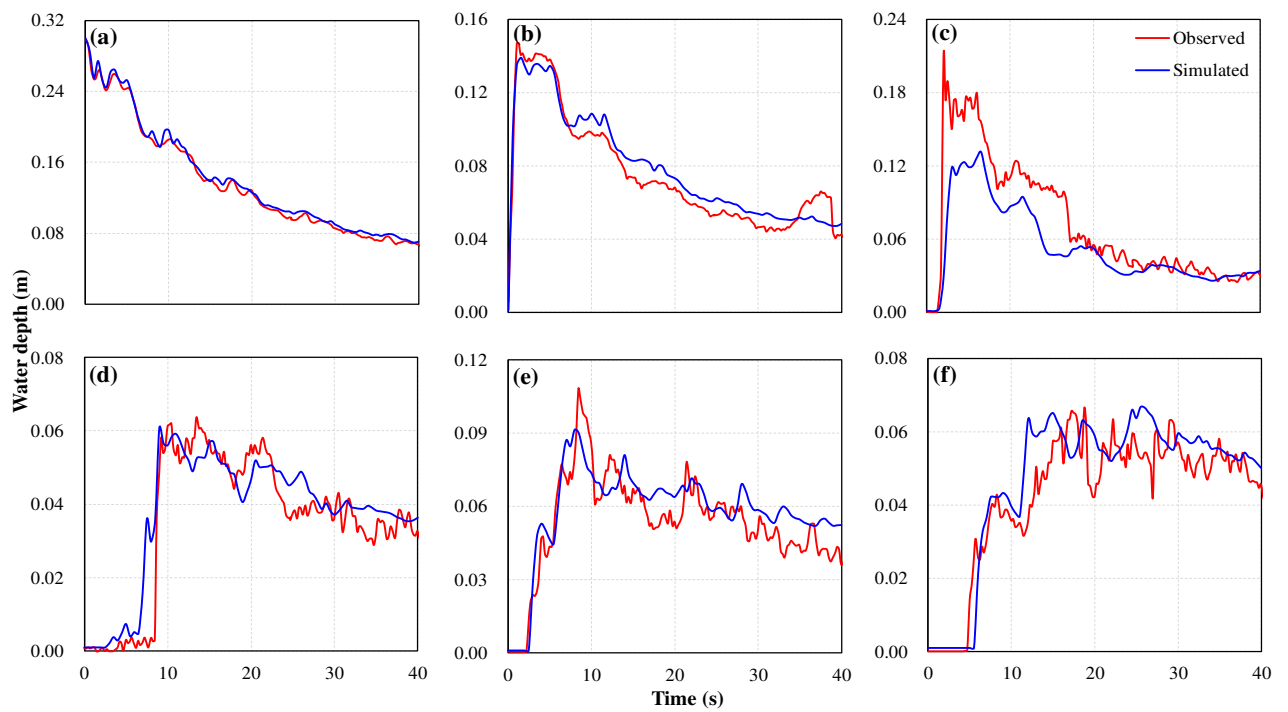
869

870

871

872

873



874

875 **Fig. 10** Comparisons between simulated and observed variations in the water depth hydrographs at

876 sites of: (a) P1; (b) P2; (c) P3; (d) P4; (e) P5; (f) P6.

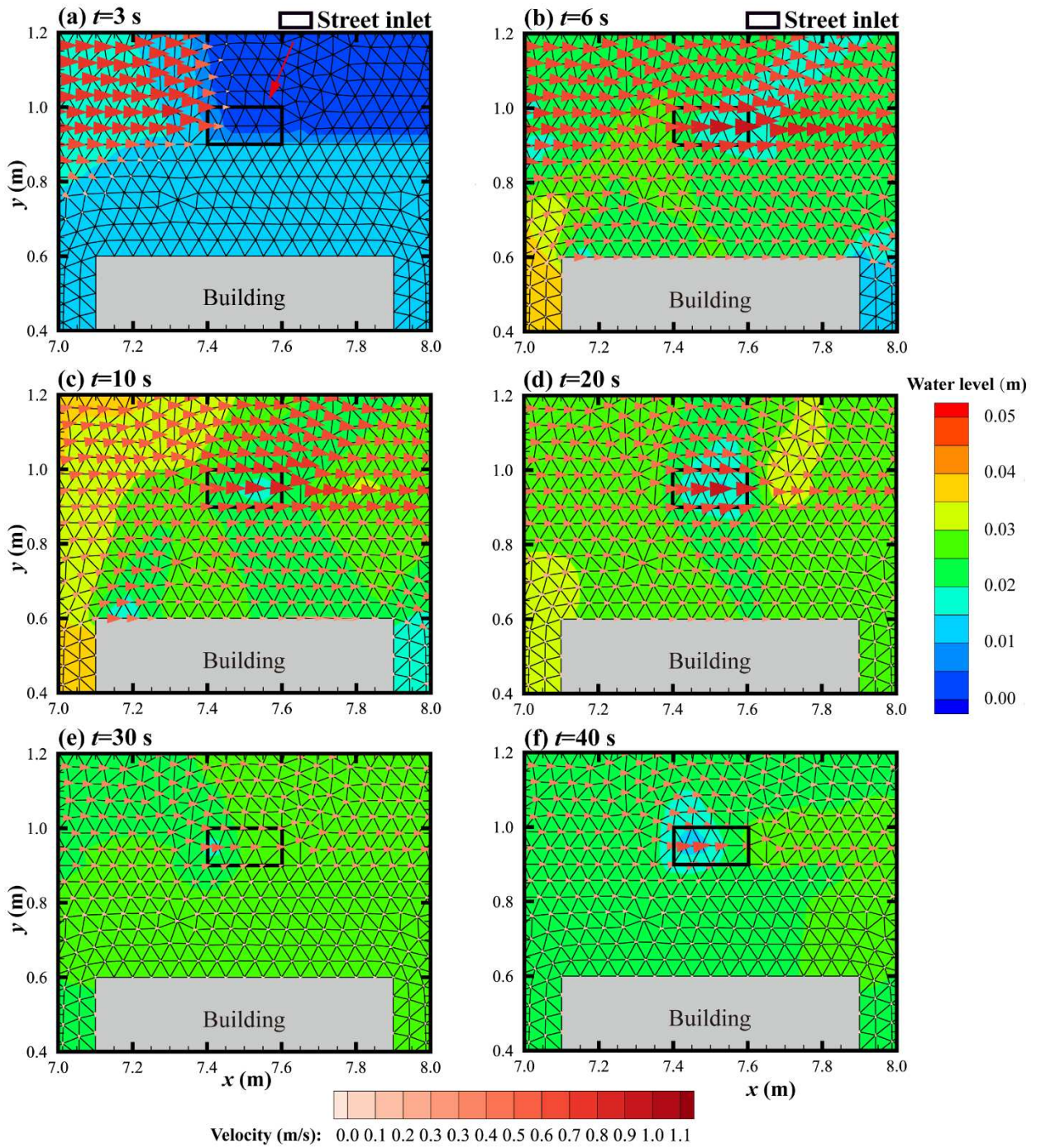
877

878

879

880

881



883

884 **Fig. 11** Velocity fields and water level distributions around the first street inlet for Case 2, for a 30

885 cm initial water depth at different times of: (a) $t=3$ s; (b) $t=6$ s; (c) $t=10$ s; (d) $t=20$ s; (e) $t=30$ s; (f)

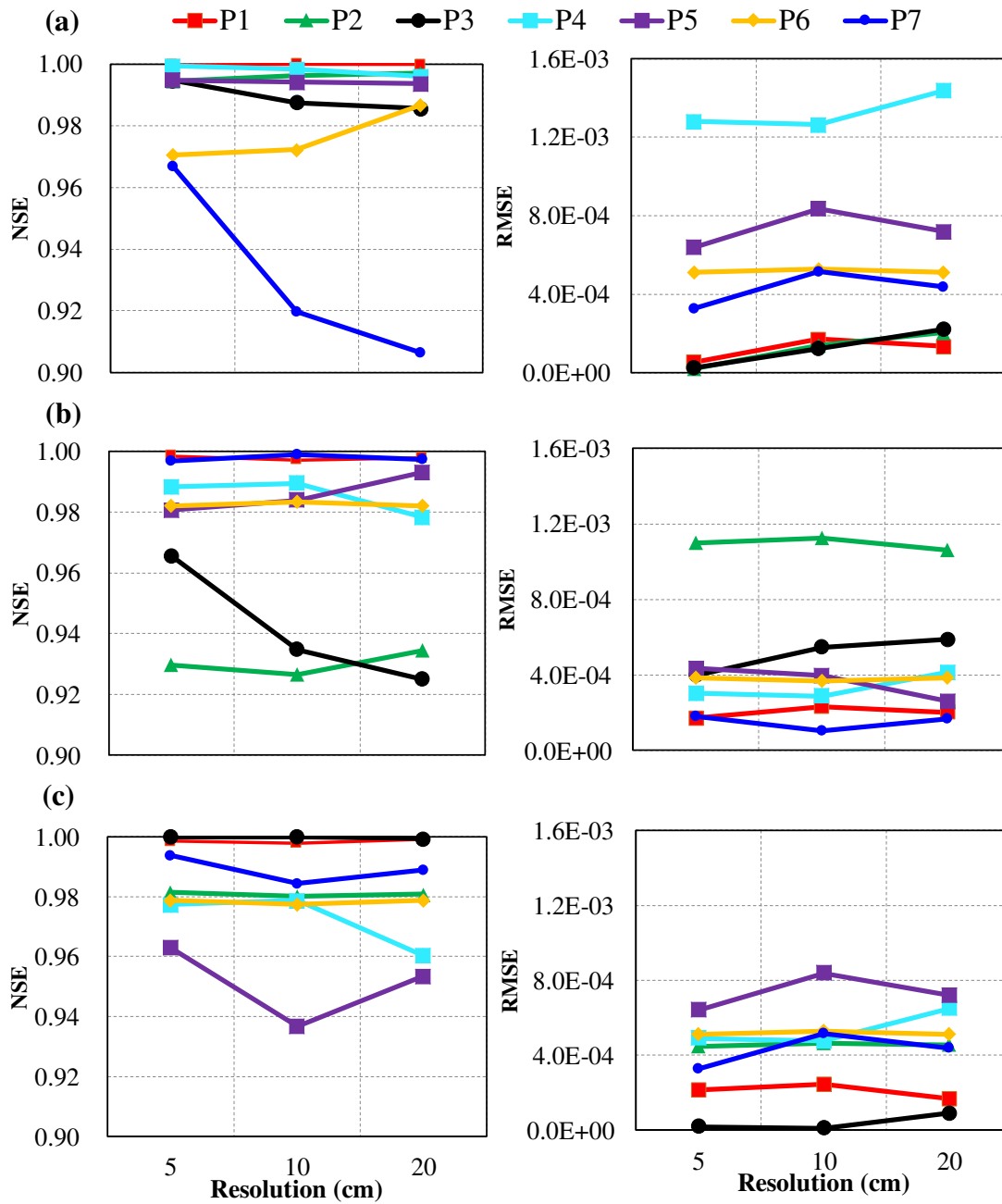
886 $t=40$ s.

887

888

889

890



891

892 **Fig. 12** Model performance variations for different mesh resolutions under initial water depths of: (a)

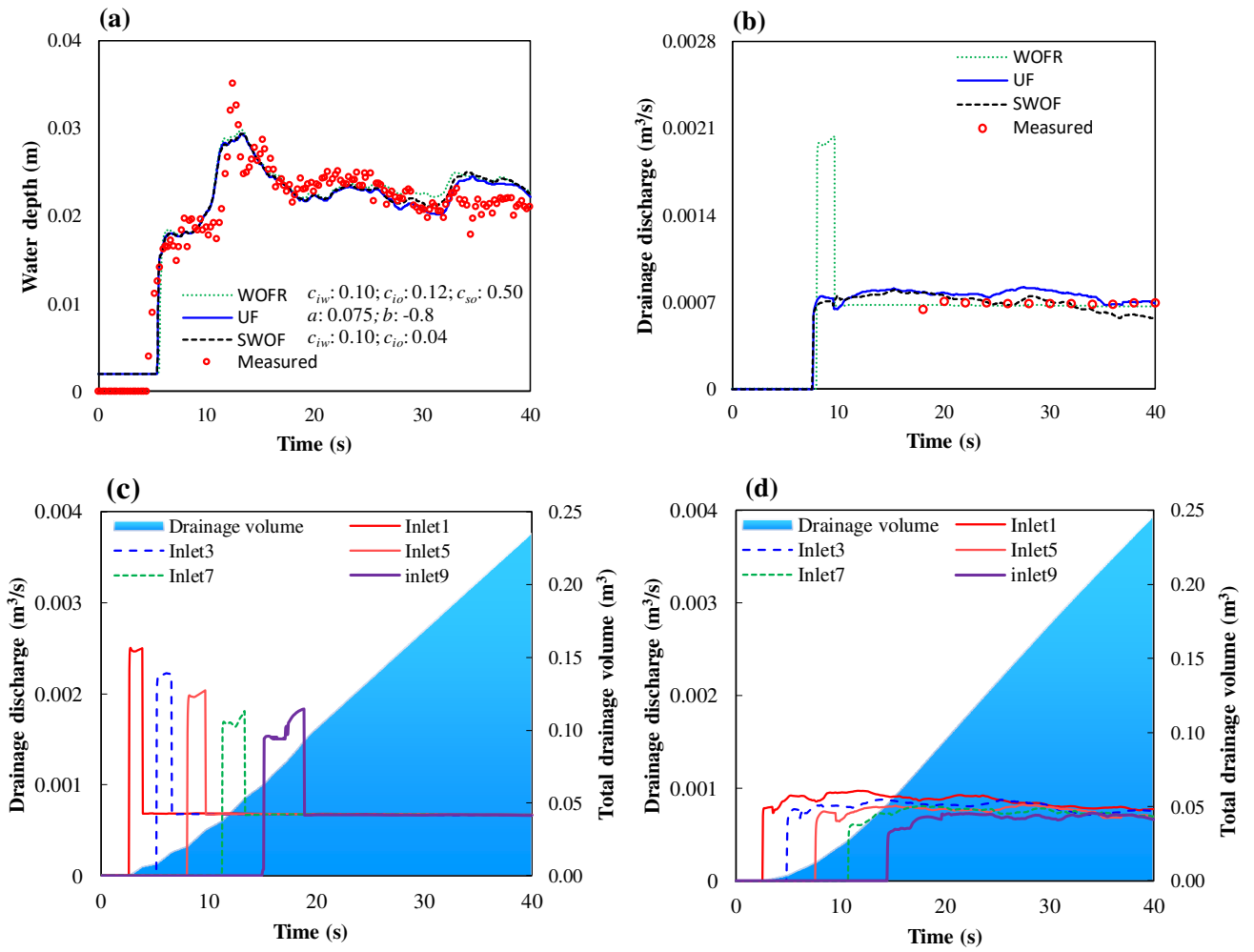
893 10 cm; (b) 20 cm; (c) 30 cm.

894

895

896

897



898 **Fig. 13** Simulated hydrographs of surface water depth, drainage discharge and total drainage volume
899 based on different discharge capacity formulae, showing: (a) surface water depth variations at P5; (b)
900 simulated and measured drainage discharges through inlet5; and (c, d) drainage discharge variations
901 along the street direction and total drainage volume obtained using the WOFR and UF, respectively.

902